Analysis of the Heterogate Electron–Hole Bilayer Tunneling Field–Effect Transistor with Partially Doped Channels: Effects on Tunneling Distance Modulation and Occupancy Probabilities

J.L. Padilla, C. Medina-Bailon, C. Navarro, C. Alper, *Student Member, IEEE,* F. Gámiz, *Senior Member, IEEE,* and A.M. Ionescu, *Senior Member, IEEE,*

***Abstract*—Within the research in bilayer tunneling field–effect transistors exploiting interband tunneling phenomena with tunneling directions aligned with gate induced electric fields, simulation results for the heterogate electron–hole bilayer TFET (HG-EHBTFET) showed that this type of devices succeeded in suppressing the parasitic tunneling leakage currents appearing in EHBTFETs as a result of the variable quatization strength inside the channel. In this paper, and conversely to standard approaches with entirely intrinsic channels, we investigate the possibility of modulating the band-to-band tunneling (BTBT) distance by acting on the subband discretization profiles through partially doped channels. We also analyze the impact of this pocket doping inside the channel on the occupancy probabilities involved in the BTBT processes in a germanium HG-EHBTFET.**

***Index Terms*—heterogate electron–hole bilayer TFET, quantum confinement, band-to-band tunneling, occupancy probabilities, steep slope transistors.**

I. Introduction

TUnneling field–effect transistors (TFETs) lie among the family of novel devices [1], [2] that seek to overcome the 60mV/dec limit from thermionic emission [3] by exploring alternative injection mechanisms based on tunneling phenomena. Extensive development and research efforts have been thereof performed for a better understanding of their working principles and suitability as steep slope switches [4], [5], [6], [7]. A particular subtype of TFETs is constituted by so-called bilayer TFETs in which band-to-band tunneling (BTBT) phenomena occur between 2-D electron and hole gases [8], [9], where the more efficient line tunneling (i.e. tunneling directions aligned with gate induced electric fields) [10], [11] is the driving actor in contrast with point tunneling TFETs where these directions are mostly perpendicular.

In this framework, the electron-hole bilayer tunneling field-effect transistor (EHBTFET) [12] was proposed as a solution for very low power operation featuring ultra sharp switching properties. However, detailed assessment of the EHBTFET demonstrated that quantum confinement effects produced diagonally oriented parasitic tunneling currents [13], [9] which degraded the transfer characteristics. As a result, innovative solutions based on counterdoping profiles inside the channel [14] and heterogate configurations modulating the quantization strength inside the channel [15] were proposed leading to restored abrupt switching with very low subthreshold swings (SS).

In spite of the above, the subband discretization of the conduction and valence bands into a discrete set of allowed energy states [16] was shown to imply a significant degradation of the ON current levels [17], [18] compared to those obtained in absence of confinement, making this issue to remain as one of the major pending drawbacks to be faced in TFETs. It has been argued too that the band bending required for attaining subband alignment in the EHBTFET would give rise to excessively high vertical electric fields induced by the gates biasing [19]. This issue could be alleviated by the arrangement of pseudobilayer structures obtaninable by the implementation of asymmetric configurations [20]. In this paper, we analyze the role that a partial doping of the channel in the germanium HG-EHBTFET plays in modulating the vertical BTBT distance between the first electron and hole subbands. This insertion of doped layers at the bottom of the channel will affect the electrostatics and, subsequently, the confinement strength inside it. Last, but not least, we analyze the implications of this pocket doping on the occupancy probabilities [21] involved in the estimation of the BTBT current.

Our work is organized as follows. In section II, we present the device structure to be analyzed compared to the conventional HG-EHBTFET with entirely intrinsic channel, and outline the simulation approach that we utilize. Sec. III assesses the impact of different thicknesses and doping profiles for the inserted channel pocket on: band profiles, BTBT distance behavior and occupancy probabilities. Finally, the main conclusions are drawn in Sec. IV.

II. Device Structure and Simulation Methodology

The structure depicted in Fig. 1(top) corresponds to a conventional germanium HG-EHBTFET featuring a source p^+

This work was supported by the European Community's Seventh Framework Programme Marie Curie Action under Grant Agreement No. 291780 (Andalucía Talent Hub), and by the Spanish Ministry of Economy under grant agreement TEC2014-59730.

J.L. Padilla, C. Medina-Bailon, C. Navarro and F. Gámiz are with the Depto. de Electrónica y Tecnología de los Computadores. Universidad de Granada. Avda. Fuentenueva s/n, 18071 Granada, Spain. (e-mail: jluispt@ugr.es).

C. Alper and A.M. Ionescu are with the Nanoelectronic Devices Laboratory, École Polytechnique Fédérale de Lausanne, Lausanne CH-1015, Switzerland.

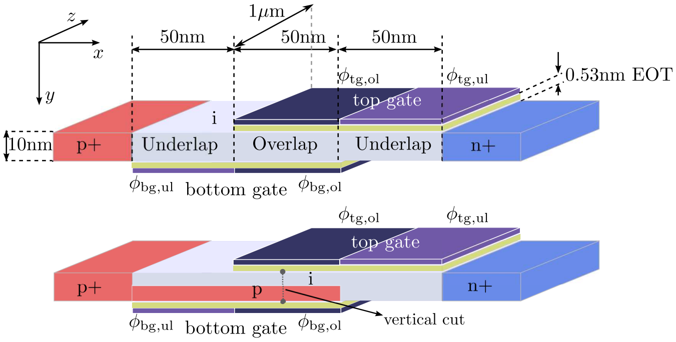

Figure 1. (Top) Schematic cross-section (not to scale) of the germanium HG-EHBTFET along with the dimensions considered in this work. The heterogate configuration suppresses parasitic tunneling contributions between overlap and underlap regions (Bottom) HG-EHBTFET featuring a p doped pocket at the bottom of the channel extending from the source to the overlap region.

region (10^{19} atoms/cm^3), intrinsic channel region with central overlap and side underlap regions (10^{15} atoms/cm^3), and drain n$^+$ region (10^{19} atoms/cm^3). The proposed configuration (bottom) shows the insertion of a variable p doped layer at the bottom of the channel ranging from the left underlap to the overlap location. The germanium body thickness is chosen to be 10nm for the results and analysis of Sec. III. Top and bottom gate dielectrics are 3nm-thick HfO_2 layers. Drain bias will be 0.3V throughout this work and bottom gate bias, $V_{\rm BG}$ set to 0V. The top gate workfunctions, $\phi_{\rm tg,ol}$ and $\phi_{\rm tg,ul}$, as well as the bottom gate workfunctions, $\phi_{\rm bg,ol}$ and $\phi_{\rm bg,ul}$ are in each case engineered so that unwanted parasitic tunneling leakage is prevented [15]. The quantization direction is along the [100] crystal orientation of Ge. Along this direction, the L electron valleys are fourfold degenerate with quantization effective mass $m_y = 0.12m_0$ and transverse effective masses $m_x = 0.15m_0$ and $m_z = 0.58m_0$. For thinner body thicknesses below 8nm [22], bulk masses for germanium are no longer valid and the effects of quantum confinement leading to bandgap and effective mass modification would need to be assessed. For the Γ valley, the effective masses of heavy holes, light holes and electrons are in our case $m_{hh} = 0.33m_0$, $m_{lh} = 0.044m_0$, and $m_{e,\Gamma} = m_{lh}$, respectively [23]. The bandgap narrowing effect inside the channel ensued from the doped pocket is accounted for by means of the Jain and Roulston model for germanium [24]. From the experimental point of view, it is clear that the fabrication of such a doping profile inside the channel would represent a significant challenge since obtaining such shallow doping profiles using ion implantation will most likely not be possible. However, similar layered structures can be achieved using epitaxial growth methods and in-situ doping [25], [26].

The simulation approach was first introduced in [13] and is based on a TCAD hybrid integration that combines the two most widely used simulators: Silvaco ATLAS (v.5.20.2.R) [27] and Synopsys Sentaurus (v.2014.09) [28]. Essentially, the simulation structure makes use of a segmented scheme in two separated steps involving one simulator at a time according to the tasks for which they show their best capabilities. As to illustrate this, we choose ATLAS to self-consistently solve the Schrödinger and Poisson equations and obtain the electrostatics derived from the inclusion of quantum mechanical confinement. The Schrödinger-Poisson model of ATLAS allows 1D and full 2D treatments and is known to offer good performance in terms of convergence compared to the 1D Schrödinger model of Sentaurus which is mostly intended for calibration purposes [28] and features frequent convergence issues [29]. In our case, and considering the large horizontal extent of the device compared to its vertical thickness, the simpler slice-by-slice 1D treatment of ATLAS turns out to be a perfectly plausible approximation.

Once the electrostatics is derived, BTBT is accounted for as a postprocessing step by means of the dynamic nonlocal BTBT model of Sentaurus [28] which dynamically calculates the tunneling paths based on the energy band profiles. This segmented simulation scheme has been demonstrated to be well-founded as long as the contribution of the injected carriers does not affect in a noticeable way the charge distribution obtained in the absence of BTBT [17], [30]. In the case of the proposed structure, both phonon assisted and direct BTBT phenomena were taken into account, along with an appropriate calibration of the tunneling paramenters [15] of the model reflecting the fact that BTBT takes place across the confinement direction of the device. The potential contribution of trap assisted tunneling at the interface between the doped slab and the intrinsic part of the channel has not been taken into account in our simulations given that its appearance and significance would depend on the experimental manufacturing procedure.

Let us clarify that in order to allow a consistent integration between both tools as for accounting for quantum confinement effects, two additional concerns need to be carefully addressed. First, the potential and charge distributions arising from the ATLAS Schrödinger-Poisson model are reproduced in Sentaurus through an appropriate calibration of the density gradient model. Second, the semiclassical edges of the conduction and valence bands in Sentaurus are readjusted via structure edition tools to make them coincident with their first subbands (namely, E_{e1} for electrons, and E_{h1} for holes), so that we succeed in simulating BTBT between bound states and not between semiclassically forbidden energy levels. Notice that E_{e1} represents the lowest subband of the L valley given that the electron effective mass for the Γ valley is very low ($m_{e,\Gamma} = m_{lh}$); and E_{h1} corresponds to the heavy holes first subband. For direct BTBT, we add up the amount $(\Delta E_{e1,\Gamma} - \Delta E_{e1})$ to the default value of 0.14eV of the $Dpath$ parameter in the dynamic nonlocal BTBT model; where $\Delta E_{e1,\Gamma}$ and ΔE_{e1} stand for the energy offsets of the first subbands in the Γ and L valleys, respectively. Shockley-Read-Hall Recombination has been also considered in our simulations and determines the OFF-state current levels. Finally, gate leakage assessment [31] has not been included in this work.

III. Results and Discussion

We make an initial choice for the gate workfunctions so that (i) subband alignment takes place below the maximum biasing for the top gate, i.e. $V_{\rm TG,align} < V_{\rm DD} = 0.3$V (except

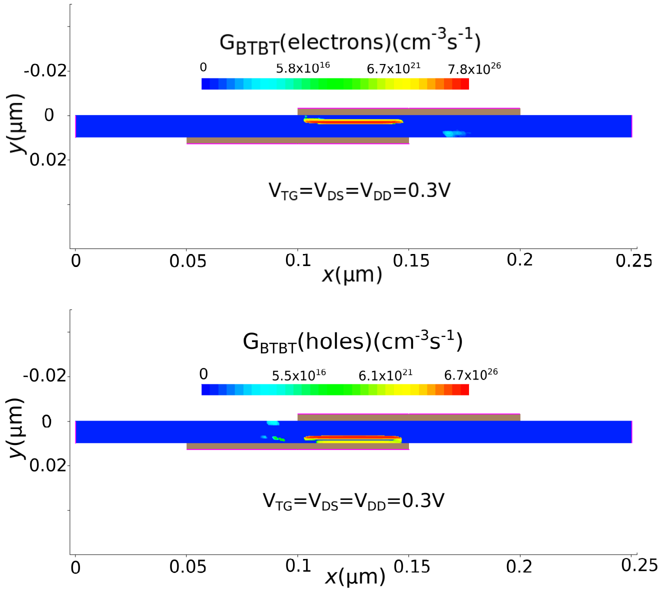

Figure 2. (Top) 2D plot of the BTBT generation rates for electrons, and (bottom) BTBT generation rates for holes for the device with $t_{\mathrm{pocket}} = 5$nm and doping of 10^{19}cm^{-3}. The spatial distribution of G_{BTBT} in both cases illustrates the pre-eminence of line tunneling phenomena as we intended to achieve with the heterogate configuration.

for the extreme case of $t_{\mathrm{pocket}} = 7$nm and 10^{20}cm^{-3} where band flattening hampers alignment); and (*ii*) parasitic diagonal tunneling currents are suppressed. In the case of the device of Fig. 1(bottom), this leads to $\phi_{\mathrm{tg,ol}} = 3.35$eV, $\phi_{\mathrm{tg,ul}} = 4.4$eV, $\phi_{\mathrm{bg,ol}} = 5.25$eV and $\phi_{\mathrm{bg,ul}} = 4.6$eV. In order to illustrate that such a heterogate configuration guarantees a scenario entirely dominated by vertical line tunneling, and prior to deepening how BTBT distance is modulated, Fig. 2 shows an example of the spatial distribution of the BTBT generation rates inside the channel at $V_{\mathrm{TG}} = V_{\mathrm{DS}} = V_{\mathrm{DD}}$ for $t_{\mathrm{pocket}} = 5$nm and 10^{19}cm^{-3}. Achieving the proposed range of workfunctions could be envisioned by using Mg (workfunction ≈ 3.6eV) for the n-gate stack and Pd or Pt (workfunctions $\approx 5.1 - 5.9$eV) for the p-gate.

A. Tunneling Distance Modulation

Fig. 3 shows (left axes) the behavior of the BTBT tunneling distance between E_{e1} and E_{h1}, d_{tunn}, along a vertical cut taken at the center of the overlap region (see Fig. 1 bottom) for different doping levels of the p-type pocket inserted at the bottom of the channel. In parallel, we show in the right axes the effect of the pocket doping on the maximum electron concentration below the top gate insulator along the same vertical cut. The results have been obtained for pocket thicknesses of t_{pocket}=3, 5 and 7nm. The curves corresponding to d_{tunn} start, in each case, at the top gate voltage at which alignment is attained, $V_{\mathrm{TG,align}}$.

We observe how a pocket doping of 10^{17}cm^{-3} provides very similar results for the three considered pocket thicknesses demonstrating that this doping level has little impact modulating the tunneling distance. On the other hand, the effect of the doped pocket proves to be noticeable for dopings

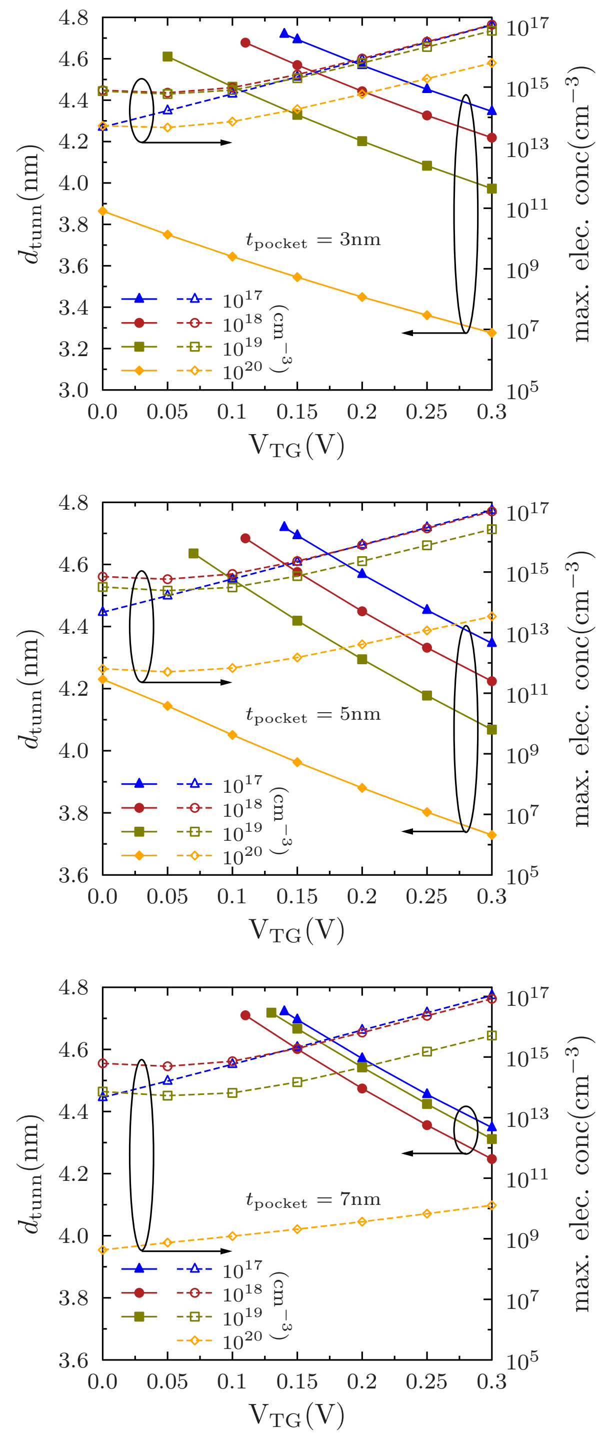

Figure 3. (Left axis) Band-to-band tunneling distance between E_{e1} and E_{h1} along a vertical cut in the center of the overlap region as a function of the applied top gate voltage for different doping levels of the inserted pocket. V_{DS} is fixed to 0.3V. No voltage is applied at the bottom gate. (Right axis) Evolution of the maximum electron concentration along the considered cut and below the top gate insulator.

of 10^{18}, 10^{19} and 10^{20}cm^{-3}. For pocket thicknesses of 3 and 5nm, an increase of the doping causes a double effect: decrease of $V_{\mathrm{TG,align}}$ and reduction of d_{tunn}. Conversely, for $t_{\mathrm{pocket}} = 7$nm the reported effect is precisely the opposite for doping values above 10^{18}cm^{-3} (i.e. increase of d_{tunn} and $V_{\mathrm{TG,align}}$); with the extreme situation of 10^{20}cm^{-3} where subband alignment is not even reached for the allowed range of V_{TG}. As for the maximum electron concentration in the vicinity of the top insulator, a rise of the pocket doping has little effect for $t_{\mathrm{pocket}} = 3$nm; whereas for $t_{\mathrm{pocket}} = 5$ and 7nm, it entails a gradual reduction, which turns out to be more pronounced as we increase the pocket thickness. In order to understand the different trends for d_{tunn} outlined above, let us show in Figs. 4 and 5 the behavior of the band profiles for $t_{\mathrm{pocket}} = 3$ and 7nm. It can be seen how an excesively thick pocket hinders the subband alignment (in fact, not attained for $t_{\mathrm{pocket}} = 7$nm and 10^{20}cm^{-3}). On the other hand, a reduced thickness combined with an increasing doping has a positive effect on the band bending leading to a reduction of the BTBT distance.

Regarding the behavior of the electric field at the insulator interfaces, one may notice that the utilization of a pocket doping of 10^{20}cm^{-3} reduces the electric field around a 15% at the bottom gate insulator as depicted in Fig. 6 (bottom). On the other hand, the effect on the electric field at the top insulator interface is not so marked except for the increase observed for $t_{\mathrm{pocket}} = 7$nm and 10^{20}cm^{-3} (consistent with the more pronounced bending of the bands reported in Fig. 5 bottom). However, this last case has little interest given that the device never reaches the ON-state in the considered range of V_{TG} (recall Fig. 3 bottommost).

Up to here, the bottom gate biasing (or, equivalently, its corresponding workfunction choice) was fixed to 0V (and $\phi_{\mathrm{bg,ol}} = 5.25$eV). We assess now the impact of $\phi_{\mathrm{bg,ol}}$ variations on the tunneling distance for $t_{\mathrm{pocket}} = 3, 5$ and 6nm. Notice that, in parallel, any modification of $\phi_{\mathrm{bg,ol}}$ would necessarily entail a consequent readjustment of $\phi_{\mathrm{tg,ul}}$ in order to avoid parasitic leakage tunneling occurring from the bottom of the overlap to the top of the right underlap [13]. The results displayed in Fig. 7 correspond to a fixed pocket doping of 10^{20}cm^{-3} and show that a reduction of $\phi_{\mathrm{bg,ol}}$ implies a decrease in d_{tunn} whose relative importance diminishes as we approach to a thickness of 3nm. In fact, although for $t_{\mathrm{pocket}} = 3$nm there is almost no impact on d_{tunn}, a closer inspection demonstrates that the trend inverts for such a reduced pocket, providing slightly bigger tunneling distances as we decrease $\phi_{\mathrm{bg,ol}}$ (this change of trend will be later on better observed in Fig. 8). In any case, and in global terms, the 3nm pocket offers the best performance for all analyzed curves. The benefits on d_{tunn} from workfunction reduction shown for $t_{\mathrm{pocket}} = 5$ and 6nm are blurred if we observe that subband alignment is gradually shifted to higher V_{TG} values.

Once that we elucidated the impact of $\phi_{\mathrm{bg,ol}}$ variations on the behavior of d_{tunn} for a fixed doping of 10^{20}cm^{-3}, let us now analyze what happens when we vary the pocket doping for a given top gate voltage, namely $V_{\mathrm{TG}} = V_{\mathrm{DD}} = 0.3$V. The results for this aim are depicted in Fig. 8. The first thing that we note is that, again, for a doping of 10^{18}cm^{-3} (and,

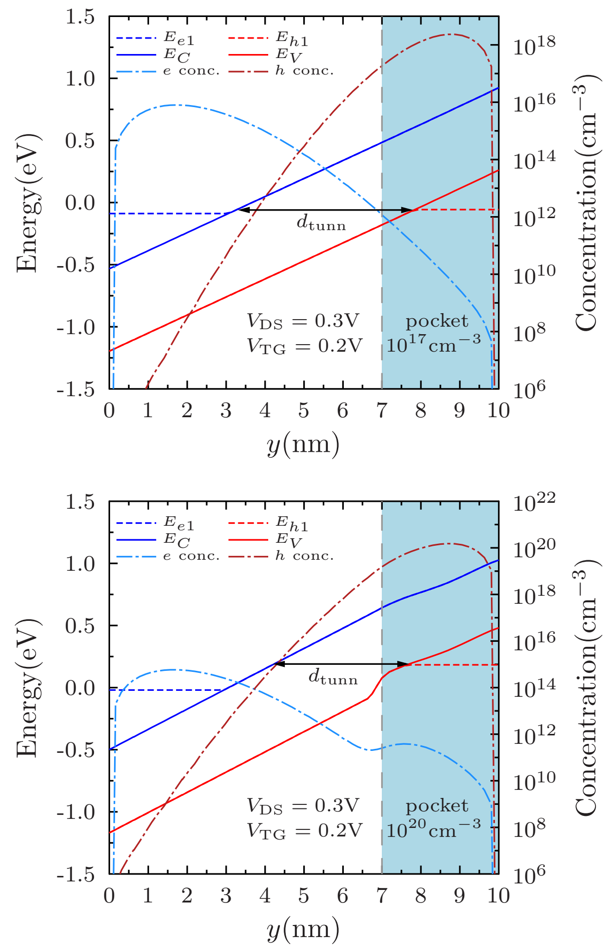

Figure 4. Band profiles (left axis) and carrier concentrations (right axis) along a vertical cut at the center of the overlap region showing the position of the first subbands for electrons and holes (dashed lines) for $t_{\mathrm{pocket}} = 3$nm. Solid lines in both figures stand for the conduction and valence band edges.

logically, below) the pocket thickness selection has very little impact on the band profile for $t_{\mathrm{pocket}} > 2$nm and, therefore, on the tunneling distance. But the most interesting thing that arises from the displayed data is that, for 10^{20}cm^{-3}, there is an inversion in the dependence of d_{tunn} on $\phi_{\mathrm{bg,ol}}$ as we vary the pocket thickness. In that sense, Fig. 8 is important to clarify an aspect that could be misinterpreted from Fig. 7, which is that one could apparently conclude that a reduction of the pocket thickness leads to the independence of d_{tunn} from $\phi_{\mathrm{bg,ol}}$ variations for a doping of 10^{20}cm^{-3}. Fig. 8 demonstrates that what actually happens is a change of trend manifested by the sign variation of the slope of orange curves. Observe that for $t_{\mathrm{pocket}} = 6$nm, the BTBT distance decreases as we lower $\phi_{\mathrm{bg,ol}}$, but this gradually changes for decreasing values of t_{pocket} till the point where, for $t_{\mathrm{pocket}} < 4$nm, this trend is inverted. Fig. 8 proves to be particularly useful as it helps to explicitly visualize the inflection point occurring between $t_{\mathrm{pocket}} = 3$ and 4nm. Notice that something similar, but somehow different, is also observable for a pocket doping of 10^{19}cm^{-3}. Similar in the sense that for a given value of $\phi_{\mathrm{bg,ol}}$, e.g. 5.15eV, the tunneling distance decreases as we

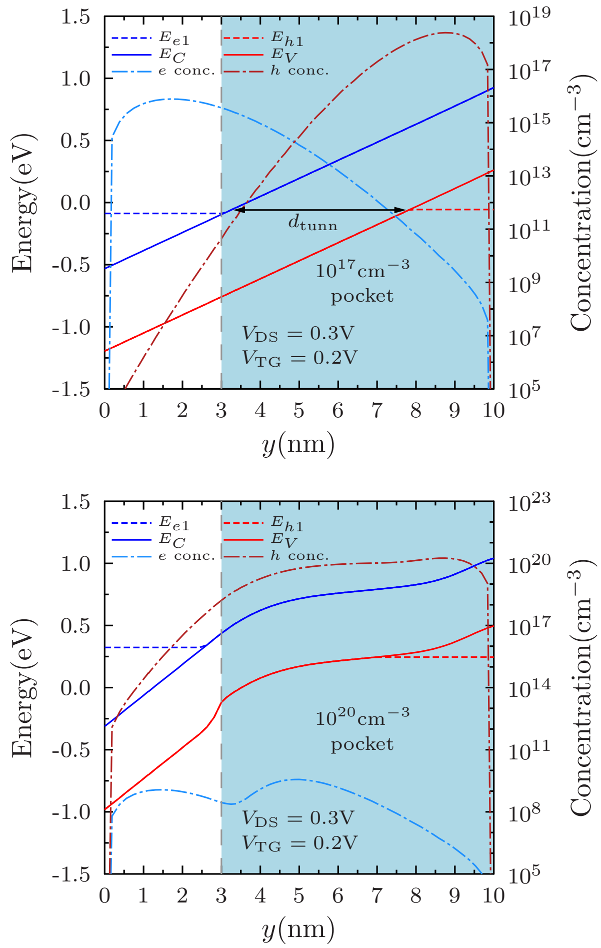

Figure 5. Band profiles (left axis) and carrier concentrations (right axis) along a vertical cut at the center of the overlap region showing the position of the first subbands for electrons and holes (dashed lines) for $t_{\rm pocket} = 7$nm. Observe how the band curvature prevents subband alignment for the case with 10^{20}cm^{-3} doping.

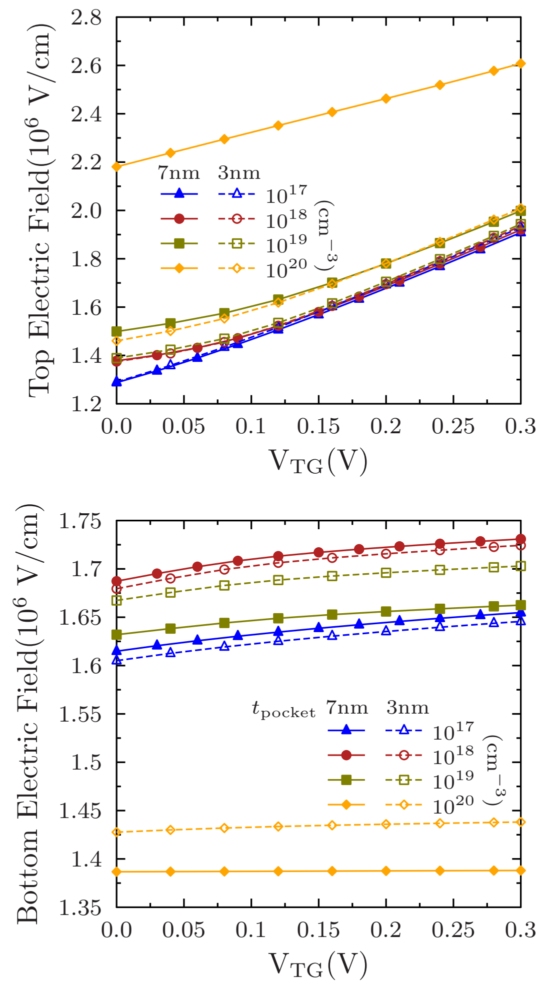

Figure 6. Electric field at the top and bottom gate insulator interfaces at the center of the overlap section for $t_{\rm pocket} = 3$ and 7nm and the different pocket dopings herein considered. Again, recall that $V_{\rm DS} = 0.3$V and $V_{\rm BG} = 0$V.

increase $t_{\rm pocket}$ starting from 2nm, but from 4nm onwards, this trend changes and $d_{\rm tunn}$ starts to grow. And different in the sense that a doping of 10^{19}cm^{-3} is not enough to make the tunneling distance decrease as we diminish $\phi_{\rm bg,ol}$ for any pocket thickness.

In light of the aforementioned changing behavior of $d_{\rm tunn}$ for fixed $\phi_{\rm bg,ol}$ (at fixed doping) observed in Fig. 8, let us know elucidate the optimal pocket thickness for each doping considering three different illustrative values of the overlap bottom gate workfunction, namely $\phi_{\rm bg,ol} = 5.05$, 5.15 and 5.35eV. The corresponding curves are shown in Fig. 9. As expected, and repeatedly noticed from previous results, $d_{\rm tunn}$ demonstrates to be slightly affected by the variation of $t_{\rm pocket}$ for a pocket doping of 10^{18}cm^{-3} (and below) . The interesting outcome arises when moving to higher dopings, given that the depicted curves allow to identify 3nm as the optimal pocket thickness minimizing $d_{\rm tunn}$. The reported slope variation corresponding to the 10^{20}cm^{-3} lines in Fig. 8 from negative to positive is clearly visible in Fig. 9 at both sides of the intersection point between the three curves ocurring at $t_{\rm pocket} = 3$nm.

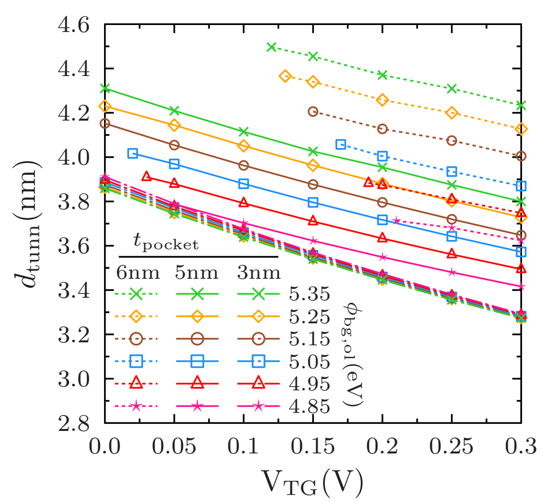

Figure 7. BTBT distance behavior as a function of $V_{\rm TG}$ for a pocket doping of 10^{20}cm^{-3} and several values of $\phi_{\rm bg,ol}$ showing the different impact that the workfunction variation entails depending on the pocket thickness. $V_{\rm DS} = 0.3$V and $V_{\rm BG} = 0$V.

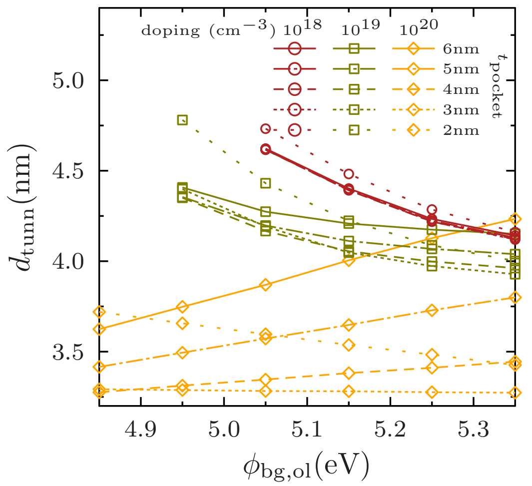

Figure 8. BTBT distance behavior as a function of $\phi_{\text{bg,ol}}$ for a fixed $V_{\text{TG}} = V_{\text{DD}} = 0.3$V showing the different impact of the pocket thickness variation depending on the pocket doping level. $V_{\text{DS}} = 0.3$V and $V_{\text{BG}} = 0$V.

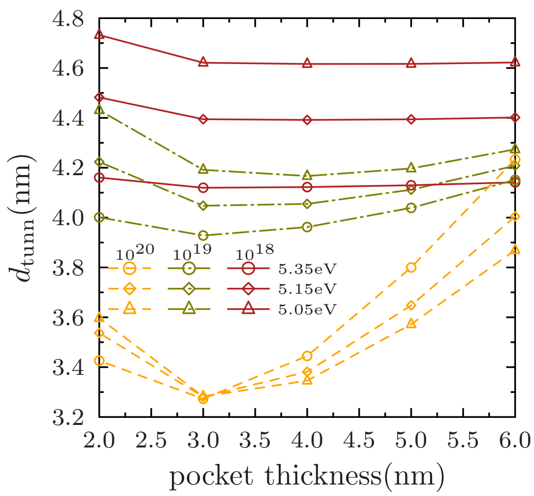

Figure 9. BTBT distance behavior as a function of t_{pocket} for a fixed $V_{\text{TG}} = V_{\text{DD}} = 0.3$V showing the impact of the different dopings depending on the chosen value of $\phi_{\text{bg,ol}}$. $V_{\text{DS}} = 0.3$V and $V_{\text{BG}} = 0$V.

B. Occupancy Probabilities Behavior

Up to here, all evidences based on BTBT distance analyses suggest that, in general terms, the optimal doping for the inserted bottom channel pocket is 10^{20}cm^{-3}. However, in the computation of the BTBT current, we also need to assess the availability of carriers at the points where tunneling starts, and the existence of empty states at the end of the tunneling paths. This means that we need to know the contributions of the Fermi-Dirac probability distributions and the density of states (DOS) at the top and bottom of the channel. As for the DOS contribution, it was stated that for a small tunneling window, it could be considered as independent of the energy [21]. Therefore, taking that approximation as valid, and making the additional assumption of a perfectly transparent tunneling barrier (i.e. BTBT probability equal to 1 in the tunneling window), we will derive a qualitative estimation of what to expect from the inclusion of partially doped channels in terms of their effect on the occupancy probabilities.

If we define I_T as the tunneling current resulting from the approximations above, it reads as

$$I_T \propto \int_{E_{e1}}^{E_{h1}} \left(f_{\text{bottom}} - f_{\text{top}}\right) dE, \qquad (1)$$

with $f_{\text{bottom(top)}}$ the Fermi-Dirac distribution at the bottom (top) of the overlap region. By performing a change of variables as done in [21], the integral can be written as a difference of complete Fermi integrals of order 0

$$\begin{aligned} I_T &\propto [F_0(\alpha) - F_0(\beta) - F_0(\gamma) - F_0(\delta)] \\ &= \ln\left\{\frac{[1+\exp(\alpha)]\,[1+\exp(\delta)]}{[1+\exp(\beta)]\,[1+\exp(\gamma)]}\right\}. \end{aligned} \qquad (2)$$

Where the arguments α, β, γ and δ are

$$\begin{aligned} \alpha &= \frac{E_{Fp,\text{bott}} - E_{e1}}{k_B T}, & \beta &= \frac{E_{Fp,\text{bott}} - E_{h1}}{k_B T} \\ \gamma &= \frac{E_{Fn,\text{top}} - E_{e1}}{k_B T}, & \delta &= \frac{E_{Fn,\text{top}} - E_{h1}}{k_B T}, \end{aligned} \qquad (3)$$

with $E_{Fp(n),\text{bott(top)}}$ standing for the hole (electron) quasi-Fermi level at the bottom (top) of the channel overlap.

Table I allows to assess the exclusive effect on I_T derived from the occupancy probability variation resulting from the pocket insertion at the bottom of the channel for thicknesses of 3 and 5nm and the workfunction choice outlined at the beginning of Sec. III. Let us recall that the results shown in Table I are obtained from the approximations that led to Eq. 1. However, although qualitative (due to the transparent barrier approximation), they are useful to show that, contrarily to the positive implications associated to the d_{tunn} reduction ensued from highly doped inserted pockets, the negative impact on the occupancy probabilities proves to be stronger for a doping of 10^{20}cm^{-3} and thicker slabs. In that sense, increasing t_{pocket} from 3 to 5nm for this highest doping shows a dramatic and harmful impact according to Table I. On the other hand, for a lower doping of 10^{18}cm^{-3}, thickening the slab proves to entail almost no impact on the occupancy probabilities.

Regarding Fig. 10, let us group the main considerations in separate points. First, given that for a doping level of 10^{18}cm^{-3}, neither d_{tunn} nor the occupancy probabilities were suffering a noticeable impact from the pocket thickness choice, its corresponding $I_{\text{DS}} - V_{\text{TG}}$ curves for $t_{\text{pocket}} = 3, 5, 7$nm prove to be almost coincident. Second, the V_{TG} values where the displayed curves turn on match the top gate voltages at which subband alignment was attained according to Fig. 3. Third, the curve for for 10^{20}cm^{-3} and $t_{\text{pocket}} = 3$nm shows a kink corresponding to the appearance of direct BTBT in germanium to the first subband of the Γ valley which boosts the current levels in comparison with indirect tunneling phenomena to the L valley. This kink can be observed for this curve given that subband alignment was strongly shifted to lower V_{TG} according to the behavior shown in Fig. 3. Fourth, since for 10^{20}cm^{-3} and $t_{\text{pocket}} = 7$nm, subband alignment

TABLE I
NUMERIC VALUES OF THE LOGARITHMIC EXPRESSION APPEARING IN EQ. 2 IN THE APPROXIMATION OF PERFECTLY TRANSPARENT BARRIER FOR $t_{\text{pocket}} = 3, 5$NM, DOPING LEVELS FROM 10^{18} TO 10^{20}CM^{-3} AND DIFFERENT TOP GATE VOLTAGES IN THE ON STATE.

Pocket Doping(cm^{-3})	$\ln\left\{\frac{[1+\exp(\alpha)][1+\exp(\delta)]}{[1+\exp(\beta)][1+\exp(\gamma)]}\right\}$					
	$V_{\text{TG}} = 0.2$V		$V_{\text{TG}} = 0.25$V		$V_{\text{TG}} = 0.3$V	
	$t_{\text{pocket}} = 3$nm	$t_{\text{pocket}} = 5$nm	$t_{\text{pocket}} = 3$nm	$t_{\text{pocket}} = 5$nm	$t_{\text{pocket}} = 3$nm	$t_{\text{pocket}} = 5$nm
10^{18}	1.759	1.742	2.817	2.764	3.780	3.730
10^{19}	2.594	1.836	3.666	2.935	4.800	4.060
10^{20}	1.150	0.013	2.059	0.040	3.114	0.114

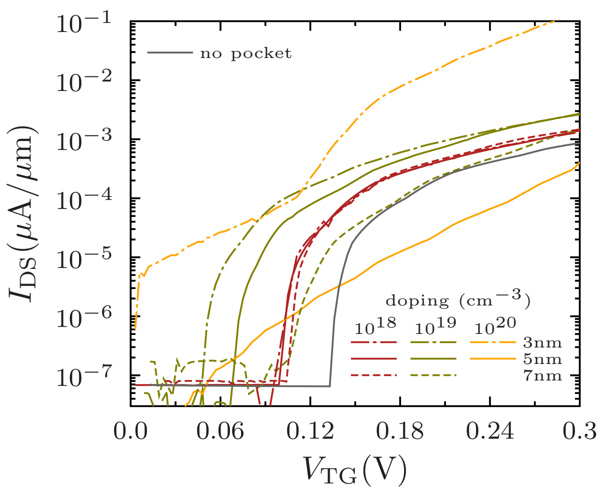

Figure 10. Transfer characteristics for the proposed HG-EHBTFET structure. The colors match those of the curves displayed in Fig. 3. $V_{\text{DS}} = 0.3$V, $V_{\text{BG}} = 0$V, $\phi_{\text{tg,ol}} = 3.35$eV, $\phi_{\text{tg,ul}} = 4.4$eV, $\phi_{\text{bg,ol}} = 5.25$eV and $\phi_{\text{bg,ul}} = 4.6$eV.

is not attained in the considered range of gate voltages, its characteristic only showed the OFF-state current and, thus, it has not been included among the displayed set of curves. Fifth, as a result of the enormous variability shown by the 10^{20} curves, this doping would need to be discarded in the optimization process. Moreover, recall that these curves were already suffering from negative effects on the occupancy probabilities. On the other hand, the doping of 10^{19}cm^{-3}, which proved to be beneficial for the occupancy probabilities, features for slab thicknesses between 3 and 5nm not very different ON-state currents and switching slopes (apart from a slight BTBT onset displacement). In that sense, we might expect pocket thickness variability not to be a critical concern for this tradeoff doping level of 10^{19}cm^{-3}. Sixth, the subthreshold slope degradation observed for the curves with 10^{20}cm^{-3} is linked to the subband profile flattening ensued from this high doping at the bottom of the channel. The reason lies in the fact that, as a result of this flattening and once alignment has been attained, the energy overlap between subbands in which BTBT is allowed grows more slowly as we increase V_{TG} compared to those cases with lower dopings where the subbands retain a sharper profile. Seventh, apart from the curve with $t_{\text{pocket}} = 3$nm and 10^{20}cm^{-3}, all the other curves feature reduced ON-state current levels as it corresponds to situations where phonon-assisted tunneling is the only type of allowed BTBT. Eighth, although apparently Fig. 10 suggests that a hypothetical displacement of the gray undoped curve (to make $V_{\text{TG,align}}$ coincident with that of the other curves) would result into very similar characteristics, it is important to mention that if we increased the maximum value of V_{TG} in that figure, thus unveiling a wider range of top gate voltages, we would observe how the gray curve saturates faster than the other curves. Therefore, such a left-shift would still provide, for example, approximately a factor x3 of improvement for the curves with 10^{19}cm^{-3} and $t_{\text{pocket}} = 3 - 5$nm over the undoped curve.

IV. CONCLUSION

In this work, we have investigated the effects of inserting a doped pocket at the bottom of the channel of a germanium HG-EHBTFET by analyzing its impact on the band-to-band tunneling distance and the occupancy probabilities behavior for the determination of the resulting drive current. We have demonstrated that, in this type of bilayer TFETs and for very high doped pockets, the negative outcome regarding the occupancy probabilities counteracts the significant reduction of the tunneling distances originally reported. The simulated results suggest that a pocket doping around 10^{19}cm^{-3} combined with a reduced pocket thickness ($\approx$ 3nm) may be an optimal choice to improve the performance of these transistors.

REFERENCES

[1] A. Ionescu and H. Riel, "Tunnel field–effect transistors as energy-efficient electronic switches," *Nature*, vol. 479, no. 7373, pp. 329–337, 2011. DOI: 10.1038/nature10679.

[2] U. E. Avci, D. H. Morris, and Y. A. Young, "Tunnel Field–Effect Transistors: Prospects and Challenges," *IEEE Journal of the Electron Devices Society*, vol. 3, no. 3, pp. 88–95, 2015. DOI: 10.1109/JEDS.2015.2390591.

[3] J. Appenzeller, M. Radosavljevic, J. Knoch, and P. Avouris, "Tunneling Versus Thermionic Emission in One-Dimensional Semiconductors," *Physical Review Letters*, vol. 92, no. 4, 2004. DOI: 10.1103/PhysRevLett.92.048301.

[4] A. C. Seabaugh and Q. Zhang, "Low-Voltage Tunnel Transistors for Beyond CMOS Logic," *Proc. IEEE*, vol. 98, no. 12, pp. 2095–2110, 2010. DOI: 10.1109/JPROC.2010.2070470.

[5] M. Schmidt, A. Schäfer, R. A. Minamisawa, D. Buca, S. Trellenkamp, J. M. Hartmann, Q. T. Zhao, and S. Mantl, "Line and Point Tunneling in Scaled Si/SiGe Heterostructure TFETs," *IEEE Electron Device Letters*, vol. 35, no. 7, pp. 699–701, 2014. DOI: 10.1109/LED.2014.2320273.

[6] G. Dewey, B. Chu-Kung, J. Boardman, J. M. Fastenau, J. Kavalieros, R. Kotlyar, W. K. Liu, D. Lubyshev, M. Metz, N. Mukherjee, P. Oakey, R. Pillarisetty, M. Radosavljevic, H. W. Then, and R. Chau, "Fabrication, Characterization and Physics of III-V Heterojunction Tunneling Field–Effect Transistors H-TFET for Steep Sub-threshold Swing," in *Proc. IEEE International Electron Devices Meeting (IEDM)*, pp. 33.6.1–33.6.4, 2011. DOI: 10.1109/IEDM.2011.6131666.

[7] D. Sarkar, X. Xie, W. Liu, W. Cao, J. Kang, Y. Gong, S. Kraemer, P. M. Ajayan, and K. Banerjee, “A subthermionic tunnel field–effect transistor with an atomically thin channel,” *Nature*, vol. 526, pp. 91–95, 2015. DOI: 10.1038/nature15387.

[8] S. Agarwal and E. Yablonovitch, “Using dimensionality to achieve a sharp tunneling FET (TFET) turn-on,” in *DRC 69th Annual*, pp. 199–200, 2011. DOI: 10.1109/DRC.2011.5994496.

[9] C. Alper, P. Palestri, L. Lattanzio, J. L. Padilla, and A. M. Ionescu, “Two Dimensional Quantum Mechanical Simulation of Low Dimensional Tunneling Devices,” *Solid-State Electronics*, vol. 113, pp. 167–172, 2015. DOI: 10.1016/j.sse.2015.05.030.

[10] Y. Lu, G. Zhou, R. Li, Q. Liu, Q. Zhang, T. Vasen, S. D. Chae, T. Kosel, M. Wistey, H. Xing, A. Seabaugh, and P. Fay, “Performance of AlGaSb/InAs TFETs With Gate Electric Field and Tunneling Direction Aligned,” *IEEE Electron Device Letters*, vol. 33, no. 5, pp. 655–657, 2012. DOI: 10.1109/LED.2012.2186554.

[11] I. A. Fischer, A. S. M. Bakibillah, M. Golve, D. Hahnel, H. Isemann, A. Kottantharayil, M. Oehme, and J. Schulze, “Silicon Tunneling Field-Effect Transistors With Tunneling in Line With the Gate Field,” *IEEE Electron Device Letters*, vol. 34, no. 2, pp. 154–156, 2013. DOI: 10.1109/LED.2012.2228250.

[12] L. Lattanzio, L. De Michielis, and A. M. Ionescu, “Complementary Germanium Electron-Hole Bilayer Tunnel FET for sub-0.5-V Operation,” *IEEE Electron Device Letters*, vol. 33, no. 2, pp. 167–169, 2012. DOI: 10.1109/LED.2011.2175898.

[13] J. L. Padilla, C. Alper, F. Gamiz, and A. M. Ionescu, “Assessment of field–induced quantum confinement in heterogate germanium electron–hole bilayer tunnel field–effect transistor,” *Applied Physics Letters*, vol. 105, no. 8, pp. 082108–1–082108–4, 2014. DOI: 10.1063/1.4894088.

[14] C. Alper, P. Palestri, J. L. Padilla, and A. M. Ionescu, “Underlap counterdoping as an efficient means to suppress lateral leakage in the electron–hole bilayer tunnel fet,” *Semiconductor Science and Technology*, vol. 31, no. 4, pp. 045001–1–045001–6, 2016. DOI: 10.1088/0268-1242/31/4/045001.

[15] J. L. Padilla, C. Alper, A. Godoy, F. Gamiz, and A. M. Ionescu, “Impact of Asymmetric Configurations on the Heterogate Germanium Electron–Hole Bilayer Tunnel Field–Effect Transistor Including Quantum Confinement,” *IEEE Transactions on Electron Devices*, vol. 62, no. 11, pp. 3560–3566, 2015. DOI: 10.1109/TED.2015.2476350.

[16] W. Vandenberghe, B. Soree, W. Magnus, G. Groeseneken, and M. Fischetti, “Impact of field-induced quantum confinement in tunneling field-effect devices,” *App. Phys. Lett.*, vol. 98, no. 14, pp. 143503–1–143503–3, 2011. DOI: 10.1063/1.3573812.

[17] A. M. Walke, A. S. Verhulst, A. Vandooren, D. Verreck, E. Simoen, V. R. Rao, G. Groeseneken, N. Collaert, and A. V. Y. Thean, “Part I: Impact of Field-Induced Quantum Confinement on the Subthreshold Swing Behavior of Line TFETs,” *IEEE Transactions on Electron Devices*, vol. 60, no. 12, pp. 4057–4064, 2013. DOI: 10.1109/TED.2013.2287259.

[18] J. L. Padilla, F. Gamiz, and A. Godoy, “A Simple Approach to Quantum Confinement in Tunneling Field–Effect Transistors,” *IEEE Electron Device Letters*, vol. 33, no. 10, pp. 1342–1344, 2012. DOI: 10.1109/LED.2012.2207876.

[19] A. Revelant, A. Villalon, Y. Wu, A. Zaslavsky, C. Le Royer, H. Iwai, and S. Cristoloveanu, “Electron–Hole Bilayer TFET: Experiments and Comments,” *IEEE Transactions on Electron Devices*, vol. 61, no. 8, pp. 2674–2681, 2014. DOI: 10.1109/TED.2014.2329551.

[20] J. L. Padilla, C. Alper, C. Medina-Bailon, F. Gamiz, and A. M. Ionescu, “Assessment of pseudo–bilayer structures in the heterogate germanium electron–hole bilayer tunnel field–effect transistor,” *Applied Physics Letters*, vol. 106, no. 26, pp. 262102–1–262102–4, 2015. DOI: 10.1063/1.4923467.

[21] L. De Michielis, L. Lattanzio, and A. M. Ionescu, “Understanding the Superlinear Onset of Tunnel-FET Output Characteristic,” *IEEE Electron Device Lett.*, vol. 33, no. 11, pp. 1523–1525, 2012. DOI: 10.1109/LED.2012.2212175.

[22] P. Rastogi, T. Dutta, S. Kumar, A. Agarwal, and Y. Chauhan, “Quantum Confinement Effects in Extremely Thin Body Germanium n-MOSFETs,” *IEEE Transactions on Electron Devices*, vol. 62, no. 11, pp. 3575–3580, 2015. DOI: 10.1109/TED.2015.2477471.

[23] K.-H. Kao, A. S. Verhulst, W. G. Vandenberghe, B. Sorée, G. Groeseneken, and K. De Meyer, “Direct and Indirect Band-to-Band Tunneling in Germanium-Based TFETs,” *IEEE Transactions on Electron Devices*, vol. 59, no. 2, pp. 292–301, 2012. DOI: 10.1109/TED.2011.2175228.

[24] S. Jain and D. Roulston, “A simple expression for band gap narrowing (BGN) in heavily doped Si, Ge, GaAs and $\mathrm{Ge}_x\mathrm{si}_{1-x}$ strained layers,” *Solid-State Electronics*, vol. 34, no. 5, pp. 453–465, 1991. DOI: 10.1016/0038-1101(91)90149-S.

[25] H.-Y. Yu, S.-L. Cheng, P. B. Griffin, Y. Nishi, and K. C. Saraswat, “Germanium *In Situ* Doped Epitaxial Growth on Si for High-Performance n+/p-Junction Diode,” *IEEE Electron Device Letters*, vol. 30, no. 9, pp. 1002–1004, 2009. DOI: 10.1109/LED.2009.2027823.

[26] Y. Moriyama, Y. Kamimuta, Y. Kamata, K. Ikeda, A. Sakai, and T. Tezuka, “In situ doped epitaxial growth of highly dopant-activated n^{+}-Ge layers for reduction of parasitic resistance in Ge-nMISFETs,” *Applied Physics Express*, vol. 7, pp. 106501–1–106501–4, 2014. DOI: 10.7567/APEX.7.106501.

[27] Silvaco *ATLAS users manual*, November 2014.

[28] Synopsys *Sentaurus Device Tool Manual*, 2014.09.

[29] G. B. Beneventi, E. Gnani, A. Gnudi, S. Reggiani, and G. Baccarani, “Optimization of a Pocketed Dual–Metal–Gate TFET by Means of TCAD Simulations Accounting for Quantization-Induced Bandgap Widening,” *IEEE Transactions on Electron Devices*, vol. 62, no. 1, pp. 44–51, 2015. DOI: 10.1109/TED.2014.2371071.

[30] C. Alper, L. Lattanzio, L. De Michielis, P. Palestri, L. Selmi, and A. M. Ionescu, “Quantum Mechanical Study of the Germanium Electron–Hole Bilayer Tunnel FET,” *IEEE Transactions on Electron Devices*, vol. 60, no. 9, pp. 2754–2760, 2013. DOI: 10.1109/TED.2013.2274198.

[31] J. T. Teherani, S. Agarwal, E. Yablonovitch, J. L. Hoyt, and D. A. Antoniadis, “Impact of Quantization Energy and Gate Leakage in Bilayer Tunneling Transistors,” *IEEE Electron Device Letters*, vol. 34, no. 2, pp. 298–300, 2013. DOI: 10.1109/LED.2012.2229458.